

Forecasting the magnitude and onset of El Niño based on climate network

Jun Meng^{1,2}, Jingfang Fan^{2*}, Yosef Ashkenazy¹, and Shlomo Havlin^{2,3}

*1 Solar Energy and Environmental Physics, Blaustein Institutes
for Desert Research, Ben-Gurion University of the Negev, Israel*

2 Department of Physics, Bar-Ilan University, Ramat-Gan 52900, Israel

*3 Institute of Innovative Research, Tokyo Institute of Technology,
4259 Nagatsuta-cho, Midori-ku, Yokohama 226-8502, Japan*

(Dated: December 3, 2024)

El Niño is probably the most influential climate phenomenon on interannual time scales. It affects the global climate system and is associated with natural disasters and serious consequences in many aspects of human life. However, the forecasting of the onset and in particular the magnitude of El Niño are still not accurate, at least more than half a year in advance. Here, we introduce a new forecasting index based on network links representing the similarity of low frequency temporal temperature anomaly variations between different sites in the Niño 3.4 region. We find that significant upward trends and peaks in this index forecast with high accuracy both the onset and magnitude of El Niño approximately 1 year ahead. The forecasting procedure we developed improves in particular the prediction of the magnitude of El Niño and is validated based on several, up to more than a century long, datasets.

PACS numbers: 92.10.am, 05.40.-a, 89.60.-k, 89.75.-k

El Niño Southern Oscillation (ENSO) is a coupled ocean-atmosphere climate phenomenon on interannual time scales [1–7]. El Niño is the warm phase of ENSO and is characterized by several degrees warming of the eastern equatorial Pacific ocean. It occurs about every 3-5 years, and is probably the most dramatic climate phenomenon on decadal time scales. It affects the surface temperature, precipitation and mid-tropospheric atmospheric circulation over extended regions in America, Australia, Europe, India, and East Asia [8–16]. In particular, strong El Niño can trigger a cascade of serious negative effects in many aspects of human life [17–20].

As a result of the environmental, economical, and social impacts of El Niño, intensive efforts have been undertaken to understand and eventually forecast El Niño [21–25]. Extensive atmospheric and oceanic observations have been used to track variations in ENSO cycle, and a whole set of complex computer models have been developed to forecast El Niño [26–39]. However, although reliable forecasts of the onset and in particular the magnitude of El Niño with relatively long lead time (of more than half a year) are critically needed, they are still missing. Here, we develop an efficient and robust framework to forecast the onset of El Niño approximately 1 year ahead, and in particular to predict the magnitude of El Niño, once it begins.

Specifically, we analyze the variability of surface air and sea temperature anomaly in the Niño 3.4 region (i.e., 5°S-5°N, 120°W-170°W) using the climate network approach [40–44]. We find that the temporal variations of temperature anomaly in different sites of the Niño 3.4 re-

gion become less coherent (more disordered) well before the onset of El Niño. Meanwhile, the magnitude of the event is proportional to the maximal degree of disorder that the Niño 3.4 region can reach before the onset of El Niño. Therefore, we are able to predict both the onset and magnitude of El Niño using a single variable, i.e., the degree of disorder (defined below) of the El Niño 3.4 region.

In the following, we first demonstrate our new forecasting method on 38 years (1979 to present) of reanalysis data of the European Centre for Medium-Range Weather Forecasts Interim Reanalysis (ERA-Interim) [45]. We then examine the robustness and accuracy of our prediction for longer periods ranging from decades to centuries using several other (reanalysis, model, etc.) datasets.

The Oceanic Niño Index (ONI) is a standard index that is used to identify El Niño [46]. It is the running 3-month mean sea surface temperature (SST) anomaly averaged over the Niño 3.4 region, based on centered 30 years periods, updated every 5 years. When the ONI exceeds 0.5°C for at least five consecutive months, the corresponding year is considered to be an El Niño year. We use the ONI (whose first value is at 1950) to estimate the accuracy of our predictions for El Niño events occurred after 1950. For three datasets, ERSST.v4 [47], PCMDI-AMIP 1.1.1 [48] and Kaplan [49], which trace back to the 1800s, we calculate the ONI based on the corresponding dataset.

We first present results that are based on the daily near surface (1000 hPa) air temperature fields of the ERA-Interim reanalysis [45]. The spatial (zonal and meridional) resolution of the data is $2.5^\circ \times 2.5^\circ$, resulting in 105 nodes in the Niño 3.4 region. We calculate the temperature anomaly by subtracting the mean seasonal cycle and dividing by the seasonal standard deviation for each

*j.fang.fan@gmail.com

grid point time series. Here, different locations in the Niño 3.4 region correspond to nodes in the local climate network, and links are determined by the similarities (defined in the next paragraph) of the temporal temperature anomaly variations between pairs of nodes [40, 50, 51].

For each pair of nodes, i and j , we calculate the cross-correlation between the two time series of 365 days as follows,

$$C_{i,j}^m(\tau) = \frac{\overline{(T_i^m(t) - \overline{T_i^m(t)})(T_j^m(t - \tau) - \overline{T_j^m(t - \tau)})}}{std(T_i^m(t))std(T_j^m(t - \tau))}, \quad (1)$$

where $T_i^m(t)$ is the temperature anomaly of node i at the time t , the overlines indicate mean values (over 365 consecutive days), $std(x)$ indicates the standard deviation of time series x , and $\tau \in [0, 200]$ days is the time lag, and m indicates the end date of the time series with 0 time shift. Then, $C_{i,j}^m(-\tau) = C_{j,i}^m(\tau)$. The similarity between two nodes (the weight of the link) is determined by the value of the highest peak of the the cross-correlation function, $C_{i,j}^m(\theta)$, where θ is the corresponding time lag at the peak. The degree of disorder/coherence of the Niño 3.4 region is quantified by the average value of all links $\langle C^m \rangle$, where higher values indicate higher coherence in the Niño 3.4 region.

The forecasting index (FI) we propose is based on the temporal evolution of $\langle C^m \rangle$ in Niño 3.4 region. We construct a sequence of networks based on monthly shifted successive windows of $200 + 365$ days. We define the FI as follows

$$FI = \overline{\ln \langle C^m \rangle} - \ln \langle C^m \rangle, \quad (2)$$

where the overline refers to average over the whole sequence of networks. Thus, it follows that the FI increases when the Niño 3.4 region is more disordered. The FI is calculated for each month (red dashed line in Fig. 1) and one can easily see that the FI increases well before the onset of El Niño, and decreases once El Niño begins. In other words, the temporal variations of temperature anomaly in different sites of the Niño 3.4 region become less coherent (more disorder) before El Niño, and start to synchronize once El Niño begins. In particular, we find that the more disordered the Niño 3.4 region is before El Niño, the higher is the magnitude of the coming El Niño.

Based on the above observation, we suggest the following algorithm to forecast both the onset and magnitude of El Niño using the FI. For demonstration see the example shown in Fig. 1 (b). We track both the FI and the ONI, starting from the onset of the previous El Niño. If the FI increases from a local minimum (“Valley”, as indicated by the blue arrow in Fig. 1 (b)) continuously for at least two months, the time at which the FI exceeds 0 is considered as a potential signal for an extreme event (El Niño/La Niña) to be initiated within the about next 18 months (“Forecast”, as indicated by

the green arrows in Fig. 1). Still, we a-priori assume that El Niño/La Niña can not be initiated during ongoing El Niño/La Niña such that the above rule does not apply during ongoing El Niño or La Niña. Moreover, if La Niña is experienced within the 18 months, we forecast a new El Niño to occur within 18 months after the end of La Niña (the first month of $T > -0.5$ after La Niña). Thus, the first forecasting signal (green arrows in Fig. 1 (a)) should be regarded only as a potential warning signal, which is confirmed after about half a year (since usually the La Niña occurs within 6 months after the potential signal). Given the above, a true-positive prediction of El Niño is counted if within 18 months after the potential signal an El Niño occurs (“normal”, as indicated by the green arrows in Fig. 1), or a La Niña that followed by an El Niño in the next 18 months occurs (“delayed”, as indicated by the green arrows with stars on the top in Fig. 1); otherwise, a false alarm is counted. The predicted magnitude of El Niño is determined by the highest peak (“Peak”, as indicated by the red points in Fig. 1 (a) and red arrow in (b)) of the FI during the period between the potential signal point (green arrows in Fig. 1) to the onset of El Niño (the end of the shaded area in Fig. 1). Only for some weak El Niño events, that the FI is monotonically increasing and we find no peak during this period.

Next, we elaborate on the reasoning behind our approach and its prediction level. In Fig. 2 (a), we plot the PDF of $C_{i,j}^m(\theta)$ for all links in networks for months at which “Valley” ($m = Valley$, blue), “Forecast” ($m = Forecast$, green) and “Peak” ($m = Peak$, red), occur. We compare these PDFs with a PDF of random networks that were obtained by shuffling the order of the years for each node inside the Niño 3.4 region. We find the strongest correlations for the “Valley” periods, then weaker correlations for the “Forecast” periods, and then the weakest correlations for the “Peak” periods (closest to the shuffled years correlations). Thus, the Niño 3.4 network (region) becomes less coherent when progressing from “Valley” periods to the “Peak” periods. The order is established toward the actual peak of El Niño. The evolution of the cross correlation of a typical link (shown in Fig. 2 (b)), before the onset of 2015-2016 El Niño event, is shown in Fig. 2 (c). The three cross correlation functions (blue, green, and red) correspond to the “Valley”, “Forecast” and “Peak” points marked by blue, green and red arrows in Fig. 1 (b). Consistently, we find that the maximal values of the cross correlation function, $C_{i,j}^m(\theta)$, decreases from time of “Valley” to “Forecast” time, then to the “Peak” time.

Moreover, while $C_{i,j}^m(\theta)$ is decreasing from Valley to Peak months, the strength of the link which as defined by $W_{i,j}^m = \frac{C_{i,j}^m(\theta) - \text{mean}(C_{i,j}^m(\tau))}{std(C_{i,j}^m(\tau))}$ [40] is increasing. This difference is probably a result of the weakening similarity of the low frequency components and unchanged simi-

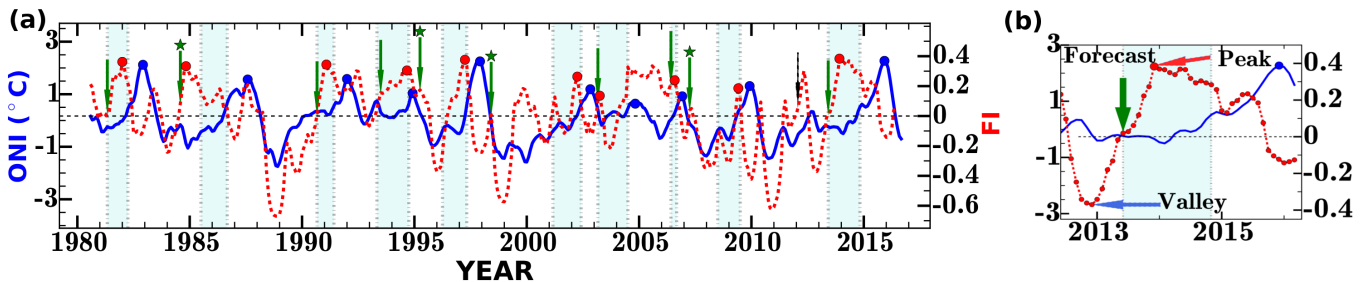


FIG. 1: (Color online) The forecasting algorithm. (a) The forecasting Index (FI, red dashed) and the ONI (blue). True positive forecasts are marked by the green arrows, while false alarms (a single point) are marked in black. The red dots are the predicted values of the magnitudes and the blue dots indicate the actual magnitudes of El Niño. The green stars above some of the green arrows indicate the predictions after which La Niña occurred, leading to postponed El Niño prediction. The horizontal black dashed line indicates $FI = 0$. (b) Detailed view of the FI and the ONI since May, 2012. The green arrow (Forecast) indicates the true positive forecast of 2015-2016 El Niño event; the blue (Valley) and red (Peak) arrows indicate the nearest minimum before the prediction point and the peak in FI that its value is used to predict the magnitude of El Niño (blue dot). The light blue shading indicates the lead time before El Niño started.

larity of high frequency components of the temperature anomaly variations in the Niño 3.4 region; see FIG. S1 in SI [52]. Thus, at the beginning of El Niño (La Niña), different nodes in the Niño 3.4 region warm (cool) together, resulting in continuously rising coherence (decreasing FI) in this region. Contrastingly, once El Niño (La Niña) declines, the warming (cooling) trend turns weak and vanishes after the termination of El Niño (La Niña), decreasing the coherence (increasing FI) in the Niño 3.4 region [53].

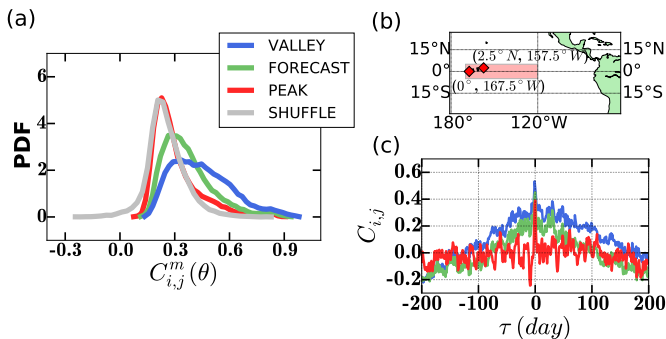


FIG. 2: (Color online) (a) PDF of $C_{i,j}^m(\theta)$ for all links within Niño 3.4 region, in networks at VALLEY (blue), FORECAST (green), PEAK (red) months (see Fig. 1), and for the random network (gray). (c) Typical cross-correlation functions of a link (shown in (b)) within Niño 3.4 region (indicated by the light red shaded area) for months of VALLEY (blue), FORECAST (green), and PEAK (red) before the 2015-2016 El Niño event.

We now examine the accuracy and robustness of our prediction for the magnitude of El Niño using several datasets that span time scales ranging from decades to centuries. For this purpose, we plot the predicted magnitude versus observed magnitude of El Niño (scatter plot), and use the Pearson correlation coefficient, r , to quantify their linear relationship. We present such scatter

plots for several datasets in Fig. 3; the correlations are relatively high ($r \geq 0.54$). Thus, our prediction of El Niño magnitude is robust, even for the longer datasets (see Fig. 3 (d) for a 144 years long dataset).

Furthermore, we apply the Kolmogorov-Smirnov test to quantify the significance of the relationship between the predicted and observed magnitude of El Niño; see FIG. S2 in the SI [52]. Each time we randomly choose ten events and calculate the correlation coefficient between their predicted and observed magnitudes; we repeated this procedure 3 million times, and obtained the PDF of r -values for each dataset. For a comparison, we also consider random cases as follows. Each time we choose randomly ten predicted values and randomly ten observed values and then perform a linear regression between them; also here we have performed 3 million selections, and obtain the PDF of r -values for each dataset. Then we compare the PDFs of observed r -values to the random r -values using Kolmogorov-Smirnov statistic,

$$D_{R,S} = \sup_r (|F_R(r) - F_S(r)|) \quad (3)$$

where $F_R(r)$ and $F_S(r)$ are the cumulative distribution functions. \sup indicates supremum. When the two cumulative distributions are identical, $D_{R,S}$ is zero and as the $D_{R,S}$ becomes larger, the observed distribution becomes more different than the random one. For each dataset used here, $D_{R,S}$ is relatively large, indicating significant relation between the observed and predicted El Niño magnitude.

The results are summarized in Table I, under the columns heading “El Niño magnitude”. Here, the lead time equals the time between the peak in the FI (which predicts the El Niño magnitude) and the peak in ONI (which determines the actual strength of El Niño). Our results suggest that usually the prediction peaks in FI lead the real peaks in ONI approximately 1 year ahead.

We note however, that the prediction of the magnitude of El Niño is performed at the actual onset of El Niño, which on average occurs about half a year prior to the peak of El Niño.

Next we examine the forecasting power of the onset of El Niño. The results are summarized in Table I, under the columns heading “El Niño onset”. Here, the hit rate is defined as the hits (true positive prediction) divided by number of El Niño events; the false alarm ratio (basically, the false discovery rate) is defined as number of false alarms divided by the sum of false alarms and hits. The lead time equals the time from the potential signal (or the end of La Niña, if La Niña is experienced after the prediction) to the actual onset of El Niño (shaded areas in Fig. 1). The resulting hit rate is relatively high (≥ 0.91) and the false alarm ratio is relatively low (≤ 0.25), for El Niño events occurred after 1950 and for all datasets examined here. For the longer datasets that span time periods of more than a century, the hit rates are also high (≥ 0.82), while the false alarms increase.

However, in the different datasets, the vast majority of the false alarms cases happened during the same period of 1920 to 1966; specifically, 27 (out of 36 false alarms), for PCMDI-AMIP 1.1.1 model [48], 18 (out of 24) for ERSST.v4 dataset [47], and 18 (out of 25) for Kaplan dataset [49]; see FIGs. S3 and S4 [52]. Moreover, even within these 46 years, we find that most of the false alarms are in certain periods when there are unusual absence of El Niño events. For example, there are no El Niño events between 1940 to 1950. Actually, it was found that the predictability of El Niño is time dependent [54–56]. In addition, the El Niño prediction during the same period exhibited lower prediction skill in a coupled oceanatmosphere model [35]. This weaker predictability skill was associated with the fewer and weaker El Niño events [35].

Previous studies proposed various methods to forecast El Niño events. Some of these predict quite successfully the onset of El Niño, about one year in advance [23, 57, 58]. The prediction scheme we proposed here does not improve significantly the prediction of the onset of El Niño. The advantage of the method we propose is that it predicts **both** the magnitude and onset of El Niño simultaneously based only on the temperature variability in the Niño 3.4 region.

In summary, we introduce a new forecasting index (FI) that is based on climate networks which accurately and simultaneously forecasts both the onset and magnitude of El Niño. The performance of the FI is examined successfully on several datasets that span time scales from decades to more than a century. Our forecasting algorithm is based on the finding that the similarity of low frequency temporal variability of temperature anomaly between different sites (strength of links) in the Niño 3.4 region decreases well before El Niño, and increases at the onset of El Niño. The magnitude of the predicted

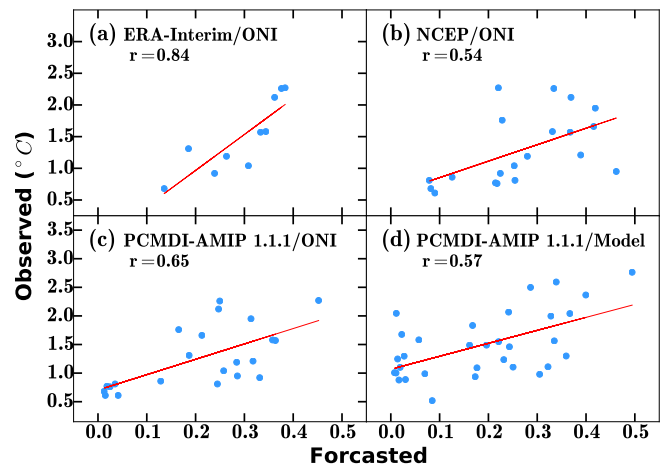


FIG. 3: (Color online) Scatter plots of the observed El Niño magnitude versus the forecast ones for different datasets (different panels). The observed strengths are obtained from ONI since 1950 in (a), since 1980 in (b) and (c), and from model Niño Index, since 1872 in (d). The different datasets are: (a) ERA-Interim, (b) NCEP reanalysis I [59], and (c), (d) PCMDI-AMIP 1.1.1. The red lines indicate linear regression fits.

El Niño is positively related with the highest peak in FI during the period between the potential alarm signal of El Niño and its actual onset. The results presented here indicate an important characteristic of the phase of the ENSO cycle, i.e., significant increase of disorder occurs in the Niño 3.4 region well before the onset of El Niño. The relationship between El Niño and the variation of the degree of disorder in the Niño 3.4 region may be further explained by defining an entropy based on the coherence of temperature variations in different sites of the Niño 3.4 region, which oscillates periodically with the ENSO cycle [61]. There is surely a room of further improvement of the forecasting algorithm proposed here, probably with combination with other forecasting techniques (e.g., current El Niño forecasting models might be improved by incorporating the results presented here).

We thank Kai Xu for helpful discussions and suggestions. The authors acknowledge the MULTIPLEX (No.317532) EU project, the Israel Science Foundation, Israel Ministry of Science and Technology (MOST) with the Italy Ministry of Foreign Affairs, MOST with the Japan Science and Technology Agency, ONR and DTRA for financial support. J.F Fan thanks the Planning and Budgeting Committee of the Council for Higher Education of Israel for financial support.

-
- [1] J. Bjerknes, *Mon. Wea. Rev.* **97**, 163 (1969).
 [2] S. E. Zebiak, M. A. Cane, *Mon. Wea. Rev.* **115**, 2262 (1987).

DATA		El Niño magnitude			El Niño onset			
Niño Index	DATASETS	r-value	$D_{R,S}$	Lead time (month)	Hit rate	False alarm ratio	Lead time (month)	
ONI	Since 1980	ERA-Interim	0.84	*	12.6 ± 9.2	(6+4)/10	1/(1+10)	12.7 ± 4.1
	Since 1960	JRA-55 [60]	–	0.45	13.2 ± 6.1	(11+6)/18	5/(5+17)	10.2 ± 5.1
	Since 1950	PCMDI-AMIP 1.1.1	0.65	0.82	10.4 ± 8.5	(16+6)/22	7/(7+22)	8.8 ± 4.8
		NCEP [59]	0.54	0.70	11.8 ± 7.6	(15+5)/22	6/(6+20)	9.4 ± 4.8
		ERSST.v4	–	0.38	9.6 ± 8.0	(14+7)/22	6/(6+21)	7.7 ± 4.5
	Kaplan	–	0.33	12.2 ± 10.2	(17+5)/22	7/(7+22)	8.2 ± 5.1	
From data	Since 1882	ERSST.v4	–	0.14	15.0 ± 9.5	(23+8)/35	24/(24+31)	7.7 ± 4.6
	Since 1872	PCMDI-AMIP 1.1.1	0.57	0.66	14.4 ± 10.9	(23+9)/37	36/(36+32)	8.6 ± 5.3
	Since 1858	Kaplan	–	0.11	16.6 ± 12.6	(23+11)/41	25/(25+34)	7.7 ± 4.7

TABLE I: Summary of the forecasting results for different datasets. The first column refers to the standard Niño Index (ONI) we use to quantify the prediction accuracy. The second column indicates the beginning year of each dataset. The third column indicates the dataset. The r -value is the Pearson correlation coefficient between the predicted and observed magnitudes of El Niño events where the “*” indicates that there are not enough events in the datasets to perform Kolmogorov-Smirnov statistic. The “–” indicates that there is no significant linear relation on the entire period of the dataset. The numerator of hit rates is composed by two parts, “normal” + “delayed”. The denominator of the false alarm ratio is composed by two parts, i.e. “falsealarms” + “hits”. In the columns of Lead time, we show the mean value ± 1 standard deviation. See more details of the above results in the Figs. S3 and S4 in the SI [52].

- [3] D. S. Battisti, A. C. Hirst, *J. Atmos. Sci.* **46**, 1687 (1989).
- [4] F. F. Jin, *J. Atmos. Sci.* **54**, 811 (1997); F. F. Jin, *J. Atmos. Sci.*, **54**, 830 (1997).
- [5] H. A. Dijkstra, *Nonlinear Physical Oceanography: A Dynamical Systems Approach to the Large Scale Ocean Circulation and El Nio* (Springer Science, New York, 2005).
- [6] A. J. Clarke *AN Introduction to the Dynamics of El Nio and the Southern Oscillation* (Academic, London, 2008).
- [7] E. S. Sarachik, M. A. Cane, *The El Nino-southern oscillation phenomenon*. (Cambridge University Press, Cambridge, UK, 2010).
- [8] M. S. Halpert, C. F. Ropelewski, *J. Clim* **5**, 577 (1992).
- [9] H. F. Diaz, M. P. Hoerling, and J. K. Eischeid, *Int. J. Climatol.*, **21**, 1845 (2001).
- [10] C. F. Ropelewski, M. S. Halpert, *Mon. Weather Rev.*, **114**, 2352 (1986).
- [11] S. Broönimann, *Rev. Geophys.* **45** (2007).
- [12] S. Power, et al. *Aust Meteor Mag* **47**, 85 (1999).
- [13] A. A. J. Williams, D. J. Karoly, N. Tapper, *Climatic Change*, **49**, 171 (2001).
- [14] K. K. Kumar, et al. *Science* **314**, 115 (2006).
- [15] C. Ihara, Y. Kushnir, M. A. Cane, and De la Peña, *Int. J. Climatol.* **27**, 179 (2007).
- [16] The data are from the Emergency Events Database (EM-DAT) of the World Health Organisation (WHO). <http://www.unocha.org/el-nino-east-africa>.
- [17] S. M. Hsiang, K. C. Meng, and M. A. Cane, *Nature* **476**, 438 (2011).
- [18] J. Currie, S. M. Rossin, *J. Health. Econ.* **32**, 487 (2013).
- [19] M. Burke, E. Gong, and K. Jones, *Econ. J.* **125**, 1157 (2015).
- [20] C. F. Schleussner, J. F. Donges, R. V. Donner, H. J. Schellnhuber, *Proc. Natl. Acad. Sci. USA* **113**, 9216 (2016).
- [21] M.J. McPhaden et al., *J. Geophys. Res.* **103**, 14169 (1998).
- [22] J.D. Neelin et al., *J. Geophys. Res.* **103**, 14261 (1998).
- [23] D. Chen, M. A. Cane, *J. Comput. Phys.* **227**, 3625 (2008).
- [24] A. von der Heydt, H. Dijkstra, *Nieuw archief voor wiskunde. Serie 5*, **14**, 195 (2013).
- [25] M.A. Cane, S.E. Zebiak, and S.C. Dolan, *Nature*, **321**, 827 (1986).
- [26] N.E. Graham, J. Michaelsen, and T.P. Barnett, *J. Geophys. Res.* **92**, 14271, (1987).
- [27] T.P. Barnett, et al., *Science* **241**, 192 (1988).
- [28] A.G. Barnston, C.F. Ropelewski, *J. Clim.* **5**, 1316 (1992).
- [29] F.T. Tang, W.W. Hsieh, and B. Tang, *Clim. Dyn.* **13**, 135 (1997).
- [30] Y. Xue, A. Leetmaa, and M. Ji, *J. Clim.* **13**, 849 (2000).
- [31] T.P. Barnett, et al., *J. Clim.* **6**, 1545 (1993).
- [32] J.D. Neelin, *J. Atmos. Sci.* **47**, 674 (1990).
- [33] M. Ji, A. Kumar, and A. Leetmaa, *Tellus* **46A**, 398 (1994).
- [34] B.P. Kirtman, et al., *Mon. Wea. Rev.* **125**, 789 (1997).
- [35] D. Chen D, M. A. Cane MA, A. Kaplan A, and S. E. Zebiak, *D. Huang, Nature*, **428**, 733 (2004).
- [36] J. J. Luo JJ, S. Masson, S. K. Behera SK, and T. Yamagata, *J. Clim.* **21**, 84 (2008).
- [37] S. W. Yeh, et al., *Nature*, **461**, 511 (2009).
- [38] M. D. Chekroun MD, D. Kondrashov D, and M. Ghil M, *Proc. Natl. Acad. Sci. USA* **108**, 11766 (2011).
- [39] E. Galanti, E. Tziperman, M. Harrison, A. Rosati A, and Z. Sirkes Z, *Mon. Wea. Rev.* **131**, 2748 (2003).
- [40] K. Yamasaki, A. Gozolchiani, S. Havlin *Phys. Rev. Lett.* **100**, 228501 (2008); A. Gozolchiani, S. Havlin, K. Yamasaki, *Phys. Rev. Lett.* **107**, 148501 (2011); Y. Wang, A. Gozolchiani, Y. Ashkenazy, Y. Berezin, O. Guez, and S. Havlin, *Phys. Rev. Lett.* **111**, 138501 (2013); D. Zhou, A. Gozolchiani, Y. Ashkenazy, S. Havlin, *Phys. Rev. Lett.* **115**, 268501 (2015);
- [41] A. A. Tsonis, K. L. Swanson, P. J. Roebber, *Bull. Amer. Meteor. Soc.* **87**, 585 (2006); A. A. Tsonis, K. L. Swanson, S. Kravtsov S, *Geophys. Res. Lett.* **34** L13705 (2007).
- [42] J. F. Donges, Y. Zou, N. Marvan, J. Kurths, *Eur. Phys. J. Spec. Top* **174**, 157 (2009); J. F. Donges, Y. Zou, N. Marvan, J. Kurths, *Europhys. Lett.* **87**, 48007 (2009).
- [43] K. Steinhäuser, N. V. Chawla, A. R. Ganguly, *SIGKDD Explor. Newsl.* **12**, 25 (2010); K. Steinhäuser, N. V. Chawla, A. R. Ganguly AR, *Statist. Anal. Data Mining* **4**, 497 (2011).
- [44] M. Barreiro, A. C. Marti, C. Masoller, *Chaos* **21**, 013101

- (2011); J. Deza, M. Barreiro, C. Masoller, *Eur. Phys. J Spec. Top* **222**, 511 (2013).
- [45] D. P. Dee, *Quarterly Journal of the Royal Meteorological Society*, **137**, 656 (2011).
- [46] <https://www.esrl.noaa.gov/psd/data/correlation/oni.data>.
- [47] B. Huang, et al., 2014: Extended Reconstructed Sea Surface Temperature version 4 (ERSST.v4): Part I. Upgrades and intercomparisons. *Journal of Climate*, in press, doi:10.1175/JCLI-D-14-00006.1;
- [48] Taylor, K.E., D. Williamson and F. Zwiers, 2000: "The sea surface temperature and sea ice concentration boundary conditions for AMIP II simulations" PCMDI Report 60, Program for Climate Model Diagnosis and Intercomparison, Lawrence Livermore National Laboratory, 25 pp available as a PDF (For further descriptive details, see <http://www-pcmdi.llnl.gov/projects/amip/AMIP2EXPDSN/BCS/index.php>).
- [49] Kaplan SST V2 data provided by the NOAA/OAR/ESRL PSD, Boulder, Colorado, USA, from their Web site at <http://www.esrl.noaa.gov/psd/>.
- [50] A. Barrat, M. Barthlemy, R. Pastor-Satorras, and A. Vespignani, *Proc. Natl. Acad. Sci. USA* **101**, 3747 (2004).
- [51] D. C. Zemp, M. Wiedermann, J. Kurths, A. Rammig, and J.F. Donges, *Europhys. Lett.* **107**, 58, 005 (2014).
- [52] See Supplemental Material for details.
- [53] However, we find that once the coherence of the Niño 3.4 region keep decreasing and reach below the average level, a new El Niño is able to form within a short period (~ 1 year), unless a La Niña is experienced beforehand (mostly within half a year) and reinitialize the onset of El Niño.
- [54] S. E. Zebiak, *J. Clim.*, **2**, 1381 (1989).
- [55] M. A. Balmaseda, M. K. Davey, and D. L. T. Anderson, *J. Clim.*, **8**, 2705, (1995).
- [56] B. P. Kirtman, P. S. Schopf, *J. Clim.*, **11**, 2804 (1998).
- [57] J. Ludescher, A. Gozolchiani, M.I. Bogachev, A. Bunde, S. Havlin, and H.J. Schellnhuber, *Proc. Natl. Acad. Sci. USA* **110**, 11742 (2013); J. Ludescher, A. Gozolchiani, M. I. Bogachev, A. Bunde, S. Havlin, and H. J. Schellnhuber, *Proc. Natl. Acad. Sci. USA* **111**, 2064 (2014).
- [58] J. Meng, J. F. Fan, Y. Ashkenazy and S. Havlin, *Chaos* **27**, 035807 (2017).
- [59] E. Kalnay et.al, *Bull. Am. Meteorol. Soc.* **77**, 437 (1996).
- [60] Japan Meteorological Agency/Japan. 2013, updated monthly. JRA-55: Japanese 55-year Reanalysis, Daily 3-Hourly and 6-Hourly Data. Research Data Archive at the National Center for Atmospheric Research, Computational and Information Systems Laboratory. <https://doi.org/10.5065/D6HH6H41>.
- [61] P. M. Saco et.al, *Physica A*, **389**, 5022 (2010).